The Astrophysical Journal, 957:45 (15pp), 2023 November 1 https://doi.org/10.3847/1538-4357/acf835

Toward a Physical Understanding of Galaxy–Halo Alignment

Kun Xu[1,2], Y. P. Jing[1,3], and Donghai Zhao[1,4]
[1] Department of Astronomy, School of Physics and Astronomy, Shanghai Jiao Tong University, Shanghai 200240, People's Republic of China; ypjing@sjtu.edu.cn
[2] Institute for Computational Cosmology, Department of Physics, Durham University, South Road, Durham DH1 3LE, UK
[3] Tsung-Dao Lee Institute, and Shanghai Key Laboratory for Particle Physics and Cosmology, Shanghai Jiao Tong University, Shanghai 200240, People's Republic of China
[4] Key Laboratory for Research in Galaxies and Cosmology, Shanghai Astronomical Observatory, Shanghai 200030, People's Republic of China
Received 2023 July 23; revised 2023 September 4; accepted 2023 September 8; published 2023 October 26

Abstract

We investigate the alignment of galaxy and halo orientations using the TNG300-1 hydrodynamical simulation. Our analysis reveals that the distribution of the 2D misalignment angle θ_{2D} can be well described by a truncated shifted exponential distribution with only *one* free parameter across different redshifts and galaxy/halo properties. We demonstrate that the galaxy–ellipticity (GI) correlations of galaxies can be reproduced by perturbing halo orientations with the obtained θ_{2D} distribution, with only a small bias ($<3°$) possibly arising from unaccounted for couplings between θ_{2D} and other factors. We find that both the 2D and 3D misalignment angles θ_{2D} and θ_{3D} decrease with ex situ stellar mass fraction F_{acc}, halo mass M_{vir}, and stellar mass M_*, while increasing with the disk-to-total stellar mass fraction F_{disk} and redshift. These dependences are in good agreement with our recent observational study based on BOSS galaxy samples. Our results suggest that F_{acc} is a key factor in determining galaxy–halo alignment. Grouping galaxies by F_{acc} nearly eliminates the dependence of θ_{3D} on M_{vir} for all three principle axes, and also reduces the redshift dependence. For θ_{2D}, we find a more significant redshift dependence than for θ_{3D} even after controlling F_{acc}, which may be attributed to the evolution of galaxy and halo shapes. Our findings present a valuable model for observational studies and enhance our understanding of galaxy–halo alignment.

Unified Astronomy Thesaurus concepts: Galaxy properties (615); Hydrodynamical simulations (767); Weak gravitational lensing (1797); Galaxy dark matter halos (1880)

1. Introduction

The intrinsic correlation between galaxy shape and the large-scale structure of the Universe has been known for a long time, know as "intrinsic alignment" (IA; Pen et al. 2000; Brown et al. 2002; Hirata et al. 2004; Mandelbaum et al. 2006; Yang et al. 2006; Okumura et al. 2009; Okumura & Jing 2009; Li et al. 2013; Singh et al. 2015; Rodriguez et al. 2022; Sheng et al. 2023; Xu et al. 2023a). IA has long be known to be a main contamination in weak lensing measurements that can result in biased constraints on cosmological parameters (Croft & Metzler 2000; Hirata & Seljak 2004; Hirata et al. 2007; Kirk et al. 2012; Krause et al. 2016). Recently, several studies suggested that IA could also serve as a promising cosmological probe in future surveys (Chisari & Dvorkin 2013; Schmidt et al. 2015; Chisari et al. 2016b; Kogai et al. 2018; Okumura & Taruya 2020, 2022), and first attempts have been made in measuring baryon acoustic oscillations (Xu et al. 2023b), redshift space distortions (Okumura & Taruya 2023), and primordial non-Gaussianity (Kurita & Takada 2023) using IA measurements. Moreover, the IA of galaxies is highly related to their formation histories since the strength of IA varies with galaxy properties such as luminosity, stellar mass, color, and morphology (Kirk et al. 2015; Singh et al. 2015; Jagvaral et al. 2022; Samuroff et al. 2022; Xu et al. 2023a). Hence, a comprehensive understanding of IA is of great importance for a wide range of cosmological and astrophysical studies.

The IA of dark matter (DM) halos is well described by the linear alignment (LA) model on large scales (Catelan et al. 2001; Hirata & Seljak 2004; Blazek et al. 2011, 2019; Okumura & Taruya 2020). The results are verified and extended to nonlinear scales using *N*-body simulations (Croft & Metzler 2000; Heavens et al. 2000; Jing 2002; Xia et al. 2017; Okumura et al. 2020). However, the IA of galaxies is much less well understood due to our limited knowledge of galaxy formation processes. Many studies found that the IA of galaxies shows a complicated dependence on galaxy and their host halo properties (Yang et al. 2006; Singh et al. 2015; Chisari et al. 2016a; Tenneti et al. 2016; Yao et al. 2020; Hoffmann et al. 2022; Jagvaral et al. 2022; Samuroff et al. 2022). To date, most IA studies focus on directly investigating the IA strength of galaxies, which is actually a combined effect of the IA of halos and galaxy–halo alignment (Bhowmick et al. 2020). Because the IA of halos is well understood, studying the alignment between galaxies and their host halos could provide more valuable insights.

In observations, there were first studies that measured the alignment between galaxies and their host halos (Okumura et al. 2009; Okumura & Jing 2009; Schneider & Bridle 2010). In these works, the misalignment angle between galaxies and their host halos are constrained by fitting the galaxy–ellipticity (GI) or ellipticity–ellipticity (II) correlation functions with an assumed distribution function. In particular, assuming a Gaussian function with zero mean for the misalignment angle distribution, Okumura et al. (2009) and Okumura & Jing (2009) reported a dispersion of 35° for luminous red galaxies (LRGs) from the Sloan Digital Sky Survey (SDSS; York et al. 2000) DR6. Xu et al. (2023a) extended this method to SDSS-III

Baryon Oscillation Spectroscopic Survey DR12 (BOSS; Alam et al. 2015; Reid et al. 2016) LOWZ, and CMASS LRG samples with the better imaging data from the DESI Legacy Imaging Surveys (Dey et al. 2019). They found that the alignment of central elliptical galaxies with their host halos increases monotonically with galaxy stellar mass or host halo mass, and that central elliptical galaxies become more aligned with their host halos as they evolve to lower redshift. They also reported a weaker alignment between disk galaxies and their host halos. For comparison, Hoffmann et al. (2022) modeled the 3D misalignment angles of the LOWZ and Dark Energy Survey (DES; The Dark Energy Survey Collaboration 2005) samples assuming a Misis–Fisher distribution, and they found nearly no luminosity or redshift dependence for central galaxies.

In theory, galaxy–halo alignment has been investigated in many works using hydrodynamical simulations. Using the Horizon-AGN simulation (Dubois et al. 2016), Chisari et al. (2017) found that the misalignment angles of the minor axes of galaxies and their host halos decrease with halo mass and increase with redshift, and the shapes of galaxies and halos are not strongly related. Tenneti et al. (2014) reported a similar halo mass dependence on major axis but with no redshift evolution in the MassiveBlack-II simulation (Khandai et al. 2015). In the EAGLE (Schaye et al. 2015) and Cosmo-OWLS (Schaye et al. 2010) simulations, Velliscig et al. (2015) also reported a halo mass dependence of the misalignment angle, but they found that early-type galaxies are more misaligned with their host halos compared to late-type galaxies, in contrast to the finding of Chisari et al. (2017). Furthermore, Velliscig et al. (2015) found that the cosine of the 2D misalignment angle can be described by a double Gaussian plus a floor with a total of five parameters, and Tenneti et al. (2014) provided a shifted exponential function with three parameters. Both studies reported that the assumption of a single Gaussian distribution may lead to an overestimation of the mean misalignment angle. However, it is hard to use either of the two models for observations since they have too many parameters. The only information from observations that can be used to constrain misalignment is suppression of the amplitudes of the GI and II correlations, which is not sufficient to break the degeneracy of the parameters.

Therefore, in this work, on one hand, we seek to develop a model that can be utilized to constrain galaxy–halo alignment in observations; and on the other hand, we aim to study the physical origin of the galaxy–halo alignment, which is still under debate. Using the TNG300-1 run from the IllustrisTNG simulations, we construct a model with only *one* free parameter to describe the 2D misalignment angle distribution, which can be applied to model the IA statistics in observations. We also investigate the dependence of the misalignment angle on various galaxy and halo properties and endeavor to identify the most fundamental parameter that governs galaxy–halo alignment. This paper is organized as follows. In Section 2, we summarize the details of the simulation. We construct a model for 2D misalignment angles in Section 3 and investigate the dependence of galaxy–halo alignment on galaxy and halo properties in Section 4. We summarize our results in Section 5.

2. Data and Methods

In this section, we provide a brief overview of the simulation used in this study, as well as the shape measurement method and galaxy/halo properties that we employ.

2.1. Hydrodynamical Simulations

We use data from IllustrisTNG[5] (Marinacci et al. 2018; Nelson et al. 2018, 2019; Naiman et al. 2018; Pillepich et al. 2018a; Springel et al. 2018), which is a suite of magneto-hydrodynamic cosmological simulations. The simulations are run by the moving mesh code AREPO (Springel 2010) and include various baryonic processes implemented as sub-grid physics (Weinberger et al. 2017; Pillepich et al. 2018b). The cosmological parameters used in the simulations are consistent with Planck results (Planck Collaboration et al. 2016): $\Omega_m = 0.3089$, $\Omega_\Lambda = 0.6911$, $\Omega_b = 0.0486$, $h = 0.6774$, $\sigma_8 = 0.8159$, and $n_s = 0.9667$. Among the simulation suite, we use the run with the largest box, TNG300-1 (hereafter TNG300). The box size is 205 h^{-1} Mpc with 2500^3 DM particles and 2500^3 gas cells, corresponding to mass resolutions of $m_{\rm DM} = 5.9 \times 10^7\, h^{-1}\, M_\odot$ and $m_{\rm gas} = 1.4 \times 10^7\, h^{-1}\, M_\odot$. The DM halos within the simulation were cataloged using friends-of-friends (FoF) methods (Davis et al. 1985), and the subhalos were cataloged using the SUBFIND algorithm (Springel et al. 2001). The simulation output is stored in 100 snapshots for redshifts between $z = 20$ and $z = 0$.

To study the evolution of the galaxy–halo alignment, we choose the nearest snapshots around five redshifts, $z = 0.0$, 0.3, 0.6, 1.0, and 1.5, in this work. To make sure galaxies are well resolved in shape, we only consider central galaxies with stellar mass $M_* > 10^{10.0}\ h^{-1}\ M_\odot$ (>1000 particles), where M_* is defined as the stellar mass within twice the stellar half-mass radius. The host DM halos of these galaxies are also well resolved in shape, which have halo mass $M_{\rm vir} > 10^{12.0}\ h^{-1}\ M_\odot$ at all redshifts, where $M_{\rm vir}$ is the viral mass of the halo (Bryan & Norman 1998).

2.2. Shapes of Galaxies and Halos

We assume that the isodensity surfaces of both galaxies and halos can be described by triaxial ellipsoids (Jing & Suto 2002). The principal axes and axial ratios of the galaxies and halos can be obtained by finding the eigenvectors and eigenvalues of their moment of inertia tensors. We use the reduced form of the inertia tensor (Bailin & Steinmetz 2005)

$$I_{ij}^{\rm 3D} = \sum_k \frac{x_{k,i} x_{k,j}}{r_k^2}, \text{ with } i, j = \{1, 2, 3\}, \quad (1)$$

where $x_{k,i}$ is the i-axis coordinate of the kth particle and r_k is the distance of the kth particle to the galaxy/halo center, which is defined as the position of the particle with the minimum gravitational potential energy.

One problem in determining the shapes is how to select the star or DM particles used to calculate the inertia tensor. We use an iteration method to achieve it (Katz 1991; Jing et al. 1995; Jing 2002). First, for galaxies, we select all the star particles within twice the stellar half-mass radius, and for their DM halos, we select all the DM particles in the central subhalos. Here we use the central subhalos rather than the whole halos to exclude substructures, which may influence the stability of the

[5] www.tng-project.org

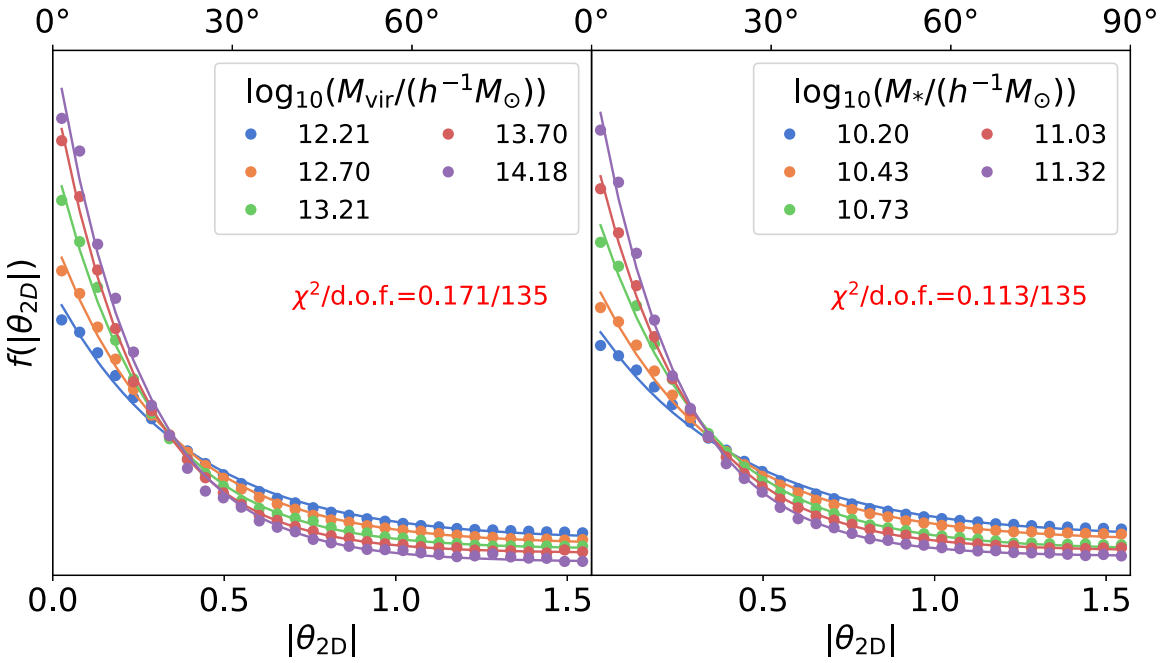

Figure 1. The distribution of $|\theta_{2D}|$ for galaxies binned by M_{vir} (left) and M_* (right) at $z = 0$. Dots show the measurements from TNG300 and lines show the best-fit TSE distribution with two free parameters, A and B.

iteration method. Then, we calculate $I_{i,j}$ and derive the three principal axes and minor-to-major (c/a) and median-to-major (b/a) axial ratios, where we respectively define the lengths of the semimajor, median, and minor axes as a, b, and c. Next, we recalculate the new principal axes and axial ratios using the particles within an ellipsoid with the principal axes and axial ratios just determined. Here we set the major axis of the ellipsoid to r_{98}, which is defined as the distance of the particle with a distance larger than 98% of the particles considered. We use r_{98} rather than the maximum distance to exclude some extreme cases. We repeat the calculation for the updated ellipsoid until the axial ratios c/a and b/a converge to an accuracy of 1%.

We also investigate the alignment of the 2D shapes of the projected galaxies and halos in this work. In this case, the iteration process is still done in 3D as above, and we use the converged particles to calculate the reduced 2D inertia tensor

$$I_{ij}^{2D} = \sum_k \frac{x_{k,i}x_{k,j}}{r_{p,k}^2}, \text{ with } i, j = \{1, 2\}, \quad (2)$$

where the inertia tensor is now reduced according to the projected distance r_p.

We have also examined our findings using the unreduced inertia tensor. We observe that the misalignment angles, on the whole, are larger when employing this definition. Nevertheless, the relationship between misalignment angle and galaxy/halo properties remains unaltered, and our conclusions remain consistent.

2.3. List of Other Properties

To understand better the physical origin of galaxy–halo alignment, we aim to study the dependence of galaxy–halo alignment on different galaxy and halo properties. We consider four specific properties in this work.

1. F_{acc}: the amount of stellar mass that was formed ex situ, i.e., accreted from galaxy mergers. This quantity is provided in the stellar assembly catalog of TNG300 (Rodriguez-Gomez et al. 2015, 2016).
2. F_{disk}: the disk-to-total stellar mass fraction. Disk particles are defined by $J_z/J(E) > 0.7$, where J_z is the specific angular momentum of the particle and $J(E)$ is the expected angular momentum for a circular orbit at the same position as that particle. See Genel et al. (2015) for more details of the definition.
3. M_{vir}: viral mass of DM halos, defined as the halo mass within the viral radius R_{vir} derived using the fitting formula from Bryan & Norman (1998).
4. M_*: stellar mass of central galaxies, defined as the stellar mass within twice the stellar half-mass radius.

3. Realistic Modeling of the 2D Galaxy–Halo Alignment

In this section, we present a model for constraining the 2D galaxy–halo alignment in observations and compare it to the approaches employed in previous studies (Okumura & Jing 2009; Xu et al. 2023a).

3.1. Truncated Shifted Exponential Distribution

There are several works that have attempted to model the 2D misalignment angle θ_{2D} between the 2D major axes of galaxies and their host DM halos using a Gaussian distribution with zero mean (Okumura et al. 2009; Okumura & Jing 2009; Xu et al. 2023a). However, it has been suggested by several studies that this assumption might not be necessarily true (Tenneti et al. 2014; Velliscig et al. 2015; Chisari et al. 2017). In Figure 1, we show distributions of θ_{2D} for galaxies binned by M_{vir} or by M_* at $z = 0$. Equal logarithmic intervals of 0.5 and 0.3 are used for dividing the halos in the mass range of $[10^{12.0}, 10^{14.5}]$ h^{-1} $M_\odot$ and the galaxies in the stellar mass range of $[10^{10.0}, 10^{11.5}]$ h^{-1} $M_\odot$. For each galaxy, we measure θ_{2D} in 1000 random projections.

Since $\theta_{\rm 2D}$ has a symmetrical distribution around 0, we only consider its absolute value $|\theta_{\rm 2D}|$. We find that the distribution of $|\theta_{\rm 2D}|$ exhibits the same form when binned by either $M_{\rm vir}$ or M_*, and can be accurately described by a truncated shifted exponential (TSE) function, similar to the distribution reported by Tenneti et al. (2014)

$$f(|\theta_{\rm 2D}|) = \begin{cases} Ae^{-|\theta_{\rm 2D}|/\tau} + B & |\theta_{\rm 2D}| \leqslant \pi/2 \\ 0 & \text{otherwise.} \end{cases} \quad (3)$$

We derive the expectation of this distribution for convenience

$$\mathbb{E}[|\theta_{\rm 2D}|] = A\tau\left(\tau - \frac{1}{2}e^{-\frac{\pi}{2\tau}}(2\tau + \pi)\right) + \frac{\pi^2 B}{8}, \quad (4)$$

and we also provide an algorithm for generating random numbers in Appendix A.

Although there are three parameters, A, B, and τ in the TSE distribution, only two of them are free due to the normalization condition $\int_0^{\pi/2} f(|\theta_{\rm 2D}|)d|\theta_{\rm 2D}| = 1$. Mathematically, it is more convenient to keep τ as a free parameter and express A or B with the other two. However, as we will demonstrate below, we aim to refine the TSE function to a distribution with a single free parameter by utilizing the empirical relations between the parameters. In this case, it is not recommended to treat τ as a free parameter since it becomes divergent when A approaches 0 and B approaches $2/\pi$. This can make it challenging to obtain a reliable value for τ. Therefore, we keep A and B as free parameters and express τ in terms of them

$$Z = \frac{A\pi}{B\pi - 2}\exp\left(\frac{A\pi}{B\pi - 2}\right), \quad (5)$$

$$\tau = -\frac{\pi(\pi B - 2)}{(4 - 2\pi B)W_0(Z) + 2\pi A}, \quad (6)$$

where W_0 refers to the principal branch of the Lambert W function W_n,[6] which can be accurately evaluated numerically[7] (Corless et al. 1996). We show in Figure 1 the best-fit TSE distribution with the two free parameters A and B for $|\theta_{\rm 2D}|$. To quantify the goodness of fit, we define χ^2 as

$$\chi^2 = \sum_i \frac{(f_i - f_i^{\rm fit})^2}{f_i^{\rm fit}}. \quad (7)$$

Here, the summation is carried out over all the bins corresponding to $|\theta_{\rm 2D}|$ used in the fitting process. We find that a TSE distribution fits the measurements very well for galaxies binned by M_* or $M_{\rm vir}$.

Currently, in observations, $\theta_{\rm 2D}$ can only be constrained by analyzing the suppression of amplitude in the GI and II correlations between galaxies and their corresponding DM halos (Okumura et al. 2009; Okumura & Jing 2009; Xu et al. 2023a). However, this information alone is insufficient to constrain the parameters fully as they can be highly degenerate. Therefore, we further reduce the degrees of freedom for A and B using empirical relations. We obtain A and B by fitting the distribution of $|\theta_{\rm 2D}|$ for galaxies binned by $M_{\rm vir}$ and M_* at different redshifts. The results are presented in Figure 2. We observe a tight correlation between A and B, which can be well described by a fitting formula of the form $B = -0.183\ln(A) + 0.336$. Therefore, we refine the TSE distribution to have only one free parameter, which is useful for modeling $\theta_{\rm 2D}$ in observations. The tight correlation between A and B suggests the possibility of a single process governing the galaxy–halo alignment, which will be explored in the next section.

To validate our TSE model, we perform additional fittings to $|\theta_{\rm 2D}|$ distributions using only one parameter, A, for galaxies binned by $F_{\rm acc}$, $M_{\rm vir}$, $F_{\rm disk}$, and M_* at $z = 0$. For $F_{\rm acc}$ and $F_{\rm disk}$, galaxies are divide into 10 equal subsamples. The fitting results are displayed in Figure 3. Remarkably, our model fits the measurements pretty well for all galaxy properties, and Figure 2 indicates that this conclusion should hold for other redshifts as well. Moreover, we observe that the alignment of galaxies and their host DM halos increases as $F_{\rm acc}$, $M_{\rm vir}$, and M_* increase, but decreases with $F_{\rm disk}$. These trends are in agreement with the real observations reported by Xu et al. (2023a), which will be explored in more detail in Section 4.

It may not be immediately apparent that the TSE distribution should be able to describe the distributions of $|\theta_{\rm 2D}|$ for galaxies with different properties. If we regard one property as a more fundamental factor in determining galaxy–halo alignment, the distribution of $|\theta_{\rm 2D}|$ for galaxies binned by other properties can be viewed as a combination of TSE distributions determined by this property, which still follows a TSE distribution. However, the sum of exponential functions is not mathematically guaranteed to be an exponential function. Nevertheless, in Appendix B, we show that for exponential functions with close exponents τ, the sum of exponential functions can still be well described by an exponential function, validating the self-consistency of the TSE model.

3.2. Modeling GI Correlation Functions

Our TSE distribution can be useful for modeling the GI and II correlations from observations and constraining the misalignment angle in the real Universe. This can be accomplished by examining the amplitude suppression in the GI and II correlations due to stochastic angular misalignment (Okumura et al. 2009; Okumura & Jing 2009; Xu et al. 2023a).

In 2D, the shapes of galaxies and halos can be described by a two-component ellipticity, which is defined as

$$e_{(+,\times)} = \frac{1 - q^2}{1 + q^2}(\cos 2\theta, \sin 2\theta), \quad (8)$$

where q is the 2D minor-to-major axial ratio of the projected shape and θ is the angle between the major axis projected onto the celestial sphere and the projected separation vector pointing to a specific object. As in Xu et al. (2023a), we set $q = 0$ for all galaxies and halos, and only care about their orientations. The $q = 0$ GI correlation is defined as

$$\tilde{\xi}_{g+}(\boldsymbol{r}) = \langle[1 + \delta_{g_1}(\boldsymbol{x}_1)][1 + \delta_{g_2}(\boldsymbol{x}_2)]e_+(\boldsymbol{x}_2)\rangle, \quad (9)$$

where $\boldsymbol{r} = \boldsymbol{x}_1 - \boldsymbol{x}_2$. This correlation can be estimated using the generalized Landy–Szalay estimator (Landy & Szalay 1993; Mandelbaum et al. 2006) with two random samples R_s and R corresponding to the tracers of ellipticity and density fields,

[6] https://en.wikipedia.org/wiki/Lambert_W_function
[7] https://docs.scipy.org/doc/scipy/reference/generated/scipy.special.lambertw.html

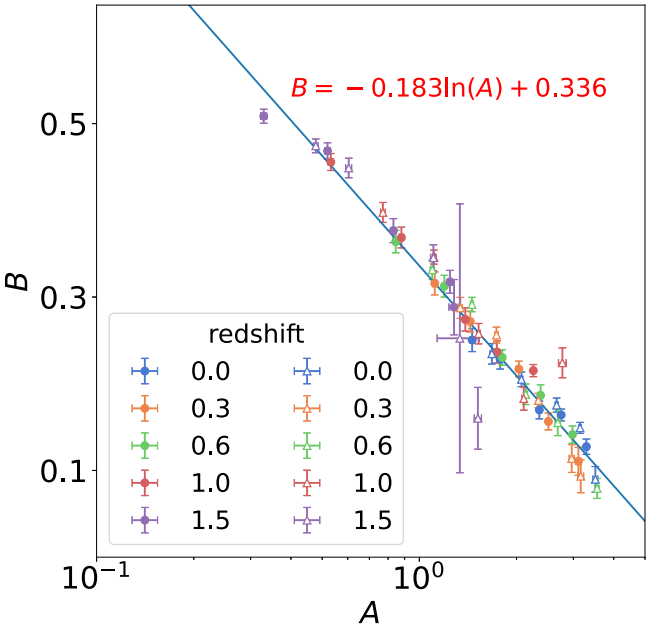

Figure 2. The best-fit parameters A and B of the TSE distribution for galaxies binned by M_* (filled circles) and $M_{\rm vir}$ (open triangles) at various redshifts. The relation between A and B can be well described by a fitting formula $B = -0.183\ln(A) + 0.336$ shown as the solid line.

respectively,

$$\tilde{\xi}_{g+}(r_{\rm p}, \Pi) = \frac{S_+(D-R)}{R_s R}, \tag{10}$$

where $R_{\rm sR}$ is the normalized counts of random pairs in a particular bin in the space of $(r_{\rm p}, \Pi)$. S_+D is the sum of the + component of ellipticity in all pairs

$$S_+D = \sum_{i,j|r_{\rm p},\Pi} \frac{e_+(j|i)}{2\mathcal{R}}, \tag{11}$$

where the ellipticity of the jth object in the ellipticity tracer is defined relative to the direction to the ith object in the density tracer, and $\mathcal{R} = 1 - \langle e_+^2 \rangle$ is the shape responsivity (Bernstein & Jarvis 2002). $\mathcal{R}$ equals 0.5 under our assumption of $q = 0$. S_+R is calculated in a similar way using the random catalog. The projected GI correlation is

$$\tilde{w}_{g_+}(r_{\rm p}) = \int_{-\Pi_{\rm max}}^{\Pi_{\rm max}} \tilde{\xi}_{g+}(r_{\rm p}, \Pi) d\Pi. \tag{12}$$

We adopt $\Pi_{\rm max} = 40\ h^{-1}$ Mpc in the following.

To constrain $\theta_{\rm 2D}$, previous studies typically recalculated $\tilde{w}_{g_+}$ for halos after perturbing the orientation of each halo according to the $\theta_{\rm 2D}$ distribution. However, as demonstrated in Blazek et al. (2011), it is possible to derive the suppression of amplitude S_2 in $\tilde{w}_{g_+}$ caused by a particular distribution of $\theta_{\rm 2D}$ analytically. Therefore, an alternative approach is to constrain the suppression S_2 and then derive $\theta_{\rm 2D}$ directly, eliminating the need to recalculate $\tilde{w}_{g_+}$ using an estimator for each $\theta_{\rm 2D}$ distribution. This method offers the advantages of being significantly faster and more stable. To establish the relation between S_2 and the distribution of $\theta_{\rm 2D}$, we introduce the alignment correlation function, $w_g(r_{\rm p}, \theta)$, which describes the dependence of clustering on both the projected separation, $r_{\rm p}$, and the orientation angle, θ, measured from the axis of separation (Faltenbacher et al. 2009)

$$\tilde{w}_{g+}(r_{\rm p}) = \frac{2}{\pi}\int_0^{\pi/2} d\theta \cos(2\theta) w_g(r_{\rm p}, \theta). \tag{13}$$

If the misalignment angle $\theta_{\rm 2D}$ is independent of θ, then

$$\begin{aligned}
&\tilde{w}_{g+}^{\rm mis}(r_{\rm p}) \\
&= \frac{2}{\pi}\int_0^{\pi/2} d\theta \int_0^{\infty} f(\theta_{\rm 2D}) d\theta_{\rm 2D} \cos[2(\theta + \theta_{\rm 2D})] w_g(r_{\rm p}, \theta) \\
&= \tilde{w}_{g+}(r_{\rm p}) \int_0^{\infty} d\theta_{\rm 2D} \cos(2\theta_{\rm 2D}) f(|\theta_{\rm 2D}|) \\
&= S_2 \tilde{w}_{g+}(r_{\rm p}),
\end{aligned} \tag{14}$$

$$S_2 = \int_0^{\infty} d\theta_{\rm 2D} \cos(2\theta_{\rm 2D}) f(|\theta_{\rm 2D}|). \tag{15}$$

Hence, once $f(|\theta_{\rm 2D}|)$ is known, the value of S_2 can be determined. For TSE

$$S_2^{\rm TSE} = \frac{A\tau(e^{-\pi/(2\tau)} + 1)}{4\tau^2 + 1}, \tag{16}$$

similarly, for a Gaussian distribution with zero mean and $\theta_{\rm 2D} \in (-\infty, \infty)$

$$S_2^{\rm Gauss} = e^{-2\sigma^2}. \tag{17}$$

The relations between S_2 and the mean $|\theta_{\rm 2D}|$ for the TSE and Gaussian distributions are shown in Figure 4. In order to achieve the same suppression S_2, the Gaussian distribution requires a slightly larger mean value of $|\theta_{\rm 2D}|$ than TSE, similar to that found in previous studies (Tenneti et al. 2014; Velliscig et al. 2015). We also confirm that the suppressed GI correlation recalculated using the estimator indeed yields the same value of S_2 as derived by Equation (15).

Figure 4 illustrates that it is always possible to find a Gaussian distribution and a TSE distribution that produce the same S_2 value, and this also holds true for any other distribution form of $\theta_{\rm 2D}$. Consequently, relying solely on $\tilde{w}_{g+}$ is insufficient to discern the distribution form of $\theta_{\rm 2D}$. It is important to note that different distribution forms of $\theta_{\rm 2D}$ can have distinct effects on $w_g(r_{\rm p}, \theta)$ and higher-order IA statistics. Here we investigate the effects on $w_g(r_{\rm p}, \theta)$ as an example. Following Blazek et al. (2011), we can expand $w_g(r_{\rm p}, \theta)$ as

$$w_g(r_{\rm p}, \theta) = w_g(r_{\rm p}) + \sum_{n\in 2\mathbb{Z}} a_n(r_{\rm p}) \cos(n\theta), \tag{18}$$

with $a_2(r_{\rm p}) = 2\tilde{w}_{g+}(r_{\rm p})$. In the LA model, where only the $\cos(2\theta)$ term is present, it is still possible to identify a Gaussian distribution and a TSE distribution of $\theta_{\rm 2D}$ that generate the same $w_g(r_{\rm p}, \theta)$. However, at nonlinear scales, where $n > 2$ terms contribute to $w_g(r_{\rm p}, \theta)$, the suppressed $w_g(r_{\rm p}, \theta)$ is

$$w_g^{\rm mis}(r_{\rm p}, \theta) = w_g(r_{\rm p}) + \sum_{n\in 2\mathbb{Z}} S_n a_n(r_{\rm p}) \cos(n\theta), \tag{19}$$

$$S_n = \int_0^{\infty} d\theta_{\rm 2D} \cos(n\theta_{\rm 2D}) f(|\theta_{\rm 2D}|). \tag{20}$$

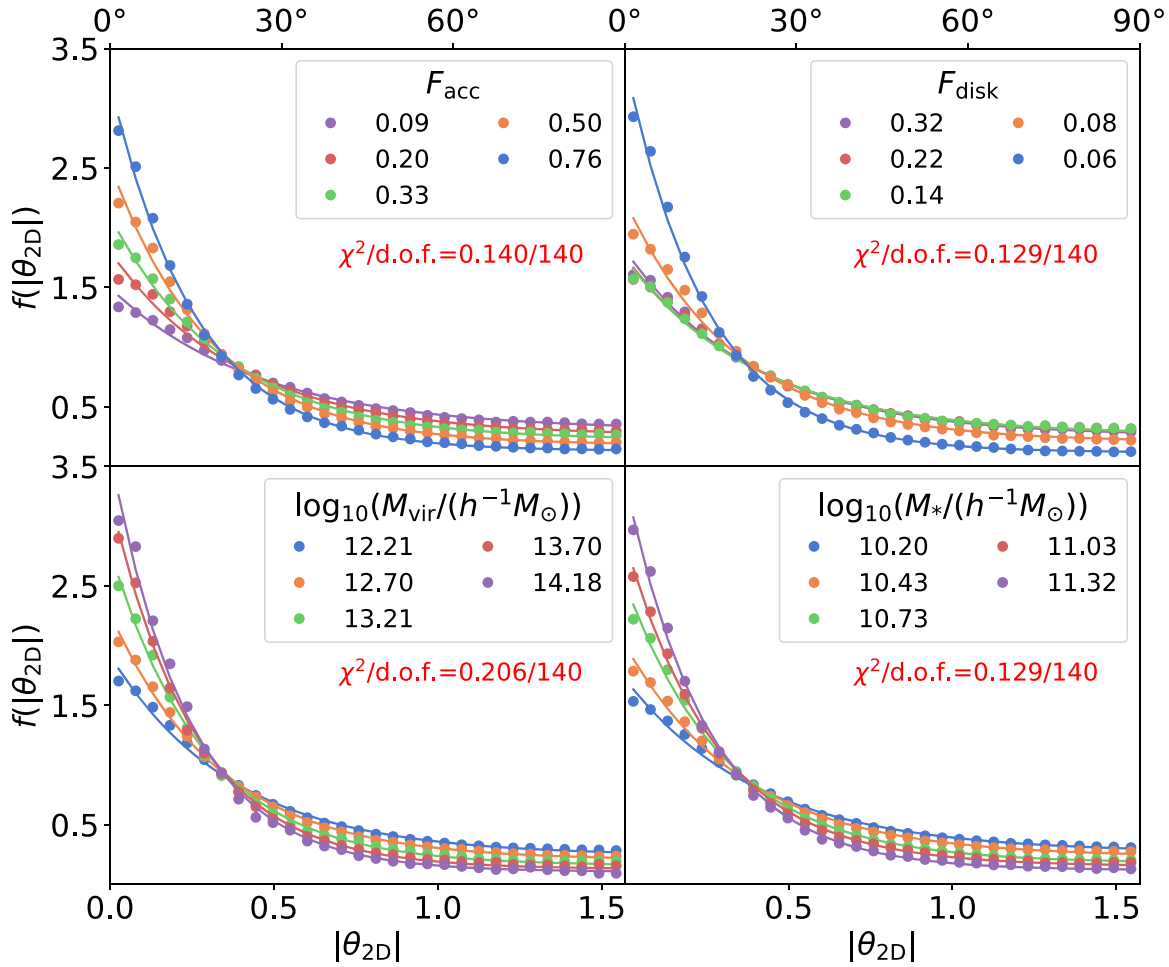

Figure 3. The distributions of $|\theta_{\rm 2D}|$ for galaxies binned by different galaxy and halo properties at $z = 0$. Dots show the measurements from TNG300 and lines show the best-fit TSE distribution with only one free parameter, A. For better illustration, we only display results from five out of the total 10 bins for $F_{\rm acc}$ and $F_{\rm disk}$.

For TSE

$$S_n^{\rm TSE} = \frac{Ae^{-\pi/(2\tau)}\tau(n\tau\sin(\frac{\pi n}{2}) - \cos(\frac{\pi n}{2}) + e^{\pi/(2\tau)})}{n^2\tau^2 + 1} + \frac{B\sin(\frac{\pi n}{2})}{n}. \quad (21)$$

For Gaussian

$$S_n^{\rm Gauss} = e^{-\frac{1}{2}n^2\sigma^2}. \quad (22)$$

It is not possible to find a Gaussian distribution and a TSE distribution that yield the same value for all S_n, allowing us to distinguish the distribution form. However, angular misalignment significantly suppresses the nonlinear terms. As a result, measuring the $n > 2$ terms for galaxies may be exceedingly difficult. Nevertheless, since $w_g(r_{\rm p}, \theta)$ remains a two-point statistic, we expect the higher-order measurements possess additional information that can be used to constrain the distribution form.

3.3. Testing the Model in TNG300

To test the validity of our method, we investigate whether the GI correlations of galaxies can be accurately reproduced by applying the best-fit $|\theta_{\rm 2D}|$ distributions to their host halos. Due to the limited volume of TNG300, we are unable to study $\tilde{w}_{g_+}$ for small stellar mass bins as done in Xu et al. (2023a). Therefore, we focus on three stellar-mass-limited samples as shape field tracers with $M_* > 10^{10.0}\ h^{-1}\ M_\odot$, $10^{10.5}\ h^{-1}\ M_\odot$, and $10^{11.0}\ h^{-1}\ M_\odot$ at $z = 0$. These samples have mean stellar

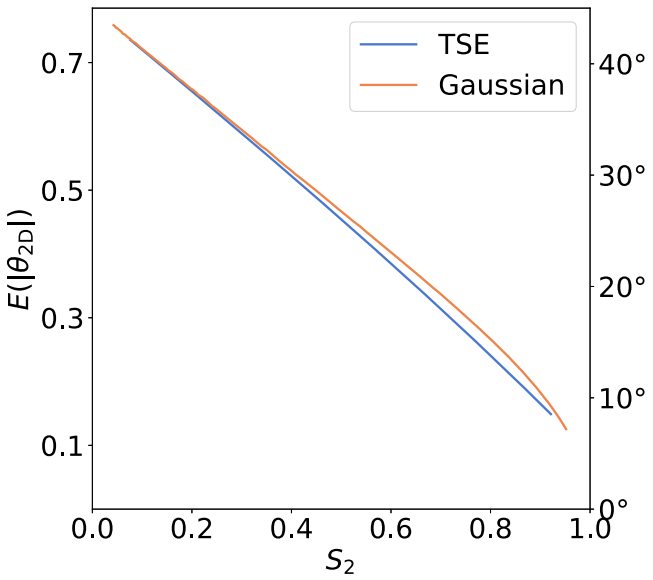

Figure 4. The relation between the suppression S_2 on $\tilde{w}_{g_+}$ and the mean $|\theta_{\rm 2D}|$ from the TSE and Gaussian distributions.

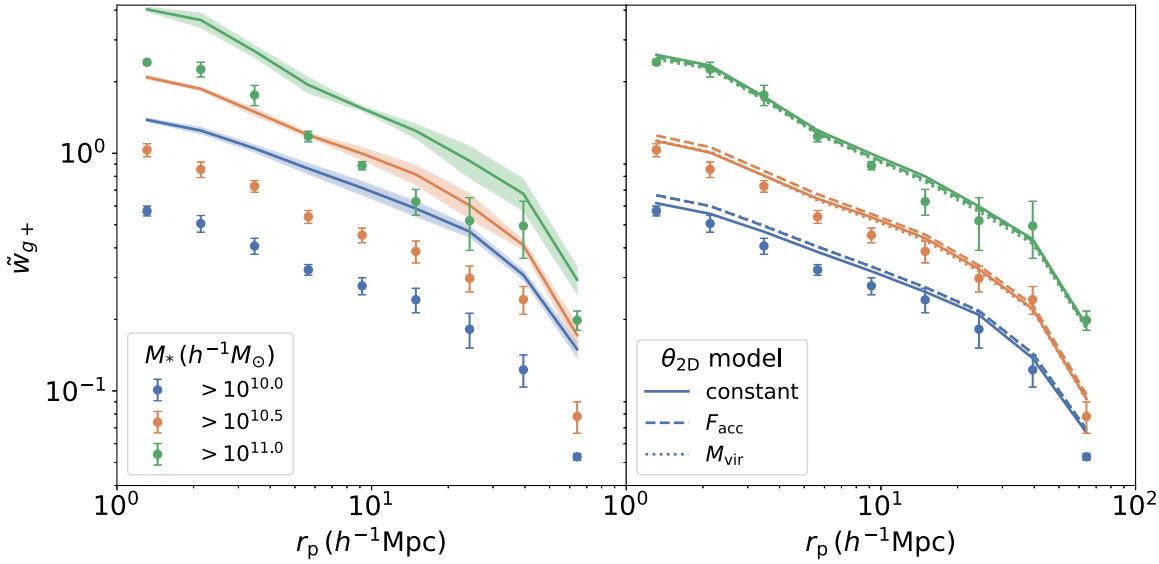

Figure 5. Left: the projected GI correlations $\tilde{w}_{g_+}$ of galaxies (dots) and halos (lines) for the three stellar-mass-limited samples at $z = 0$. Right: $\tilde{w}_{g_+}$ of halos after suppressing the amplitudes with 2D misalignment angles from different models: a constant TSE model (solid lines), an $F_{\rm acc}$-dependent TSE model (dashed lines), and an $M_{\rm vir}$-dependent TSE model (dotted lines). The results are compared with the $\tilde{w}_{g_+}$ of their galaxies (dots).

masses of $10^{10.47}\ h^{-1}M_\odot$, $10^{10.80}\ h^{-1}\ M_\odot$, and $10^{11.27}\ h^{-1}\ M_\odot$, respectively. To improve the measurements, we use all halos with more than 50 particles at $z = 0$ as the density field tracers for all three shape samples.

We present the $\tilde{w}_{g_+}$ measurements of galaxies and their host halos in the left panel of Figure 5. The mean values and errors of $\tilde{w}_{g_+}$ are estimated from three different projection directions. Our results indicate that galaxies have lower $\tilde{w}_{g_+}$ than their host halos, which is expected due to the misalignment. Furthermore, we observe that more massive galaxies and their host halos exhibit a larger $\tilde{w}_{g_+}$, consistent with previous studies (Jing 2002; Xia et al. 2017).

Subsequently, we explore whether suppressing the amplitude of the $\tilde{w}_{g+}$ of the host halos, based on the TSE distributions of $|\theta_{\rm 2D}|$, can accurately reproduce the $\tilde{w}_{g+}$ of their corresponding galaxies. We consider three different models: a constant TSE model, an $F_{\rm acc}$-dependent TSE model, and an $M_{\rm vir}$-dependent TSE model. In the constant TSE model, the suppression is calculated by the TSE distribution obtained by fitting the $|\theta_{\rm 2D}|$ of the entire sample, which has $\mathbb{E}(|\theta_{\rm 2D}|) = 0.49$, 0.43, and 0.35 for $M_* > 10^{10.0}\ h^{-1}\ M_\odot$, $10^{10.5}\ h^{-1}\ M_\odot$, and $10^{11.0}\ h^{-1}\ M_\odot$, respectively. For the $F_{\rm acc}$- and $M_{\rm vir}$-dependent models, we use the best-fit relations based on the results in Figure 3: $\mathbb{E}(|\theta_{\rm 2D}|) = -0.33F_{\rm acc} + 0.60$ and $\mathbb{E}(|\theta_{\rm 2D}|) = -0.11M_{\rm vir} + 1.83$. For the constant TSE model, the suppression S_2 is calculated using Equation (16). In the $F_{\rm acc}$- and $M_{\rm vir}$-dependent models, we recalculate the correlations using the estimator after perturbing the orientation of each halo, although, in principle, they can also be derived analytically.

The results are shown in the right panel of Figure 5. We find that the suppressed GI correlations of the halos from all three misalignment models can basically match the GI correlations of galaxies, but the amplitudes are slightly higher. The results from the three different models are consistent with each other, indicating that the GI correlations are not sensitive to the variation of the misalignment angle distribution between halos and are mainly determined by the overall distribution. Despite the good agreement, the small residuals suggest that there may exist unknown couplings between the misalignment angles and other factors, such as coupling with galaxy or halo shapes as reported by Okumura & Jing (2009) and Blazek et al. (2011). Nevertheless, as we will show below, this model is already accurate, with only a 3° bias for the worst case. We leave a detailed investigation of the mismatch to future works.

We further constrain the misalignment angles of the three stellar-mass-limited samples by fitting their $\tilde{w}_{g_+}$ using the constant TSE model and compare them to the results obtained from direct counting and fitting the $|\theta_{\rm 2D}|$ distribution. We also include the fitting results using a Gaussian model with zero mean as used in previous works (Okumura et al. 2009; Okumura & Jing 2009; Xu et al. 2023a) for comparison. The results are presented in Figure 6. The left panel shows that both the TSE and Gaussian models provide a good fit to the $\tilde{w}_{g_+}$ of the galaxies, and in the right panel, we observe that the Gaussian model requires slightly larger values ($\sim$1°) of the mean $|\theta_{\rm 2D}|$ than the TSE model to achieve the same suppression for fitting the $\tilde{w}_{g_+}$ of galaxies, as expected from Figure 4. We again demonstrate that the TSE model provides a good fit to the $|\theta_{\rm 2D}|$ distribution, as shown by comparing the fitting results to the direct counting results. The results from fitting the $\tilde{w}_{g_+}$ with the TSE model are slightly higher ($<$3°) than those obtained from direct counting and fitting the distribution, which is consistent with the results in Figure 5.

In summary, our TSE model reproduces the galaxy GI correlations well, with only a small bias, and has the potential to be useful for modeling galaxy–halo alignment in observational studies.

4. Dependence on Galaxy/Halo Properties

Recently, using observations, Xu et al. (2023a) discovered that galaxies with larger stellar mass M_* or host halo mass $M_{\rm vir}$ and at lower redshifts are more aligned with their host halos, though they focus mainly on massive galaxies ($M_* > 10^{11.0}\ M_\odot$). They also observe that elliptical galaxies are considerably more aligned with their halos compared to disk galaxies. These trends are already evident in Figure 3 in TNG300. In this section, we aim to investigate the

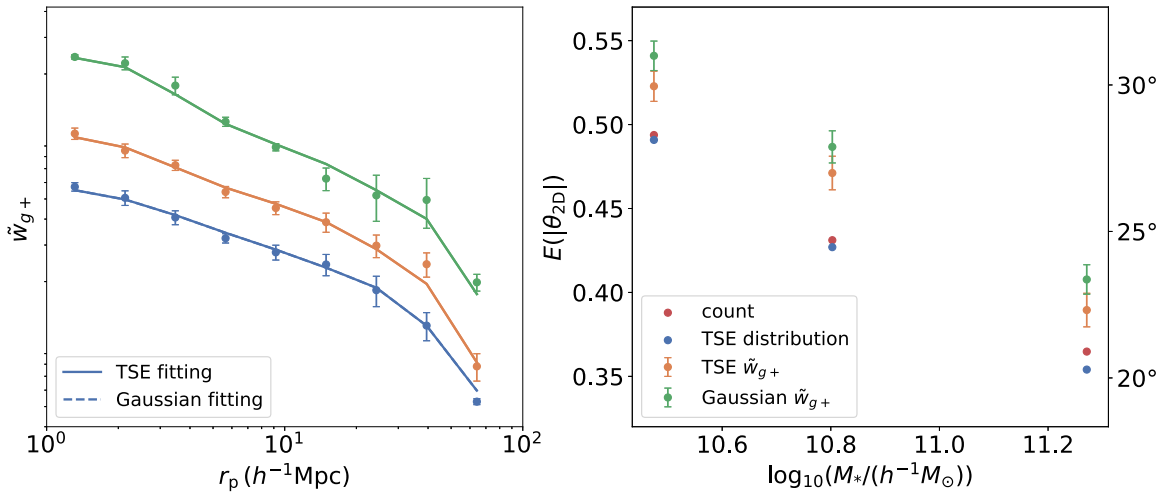

Figure 6. Left: comparison between the galaxy and best-fit halo $\tilde{w}_{g_+}$ using both the TSE and Gaussian misalignment models. Right: mean $|\theta_{2D}|$ obtained from different methods: direct counting (red), fitting the $|\theta_{2D}|$ distribution with the TSE model (blue), fitting the $\tilde{w}_{g_+}$ with the TSE model (orange), and fitting the $\tilde{w}_{g_+}$ with the Gaussian model (green).

dependence of the galaxy–halo alignment on various galaxy or halo properties further, both in 2D and 3D.

4.1. 3D Misalignment Angle

We first investigate the 3D misalignment angle θ_{3D} for all three principal axes. Since we have not found a model that accurately describes the distribution of θ_{3D}, we directly calculate the mean value of $\cos(\theta_{3D})$ for each property and at each redshift. We use $\cos(\theta_{3D})$ instead of θ_{3D} because θ_{3D} occupies different differential volumes.

In Figure 7, we show the mean $\cos(\theta_{3D})$ of the three principle axes for galaxies with different properties and at different redshifts. We find that galaxies are more aligned with their host halos for larger F_{acc}, M_{vir}, and M_*, and smaller F_{disk} for all three principle axes, although the mean $\cos(\theta_{3D})$ seems to remain constant for $F_{disk} > 0.2$. Galaxies at lower redshifts are also more aligned with their host halos. An important question that arises is which parameter is more closely related to the origin of the alignment between galaxies and their host halos. To answer this question, we want to point out that the redshift evolution of the mean $\cos(\theta_{3D})$ is much weaker when galaxies are binned by F_{acc} than when they are binned by M_{vir} and M_*, as shown in Figure 7. Specifically, for the major axis, when binned by F_{acc}, the redshift dependence is nearly eliminated for $F_{acc} > 0.5$. Although similar results are also found for $F_{disk} < 0.1$, there is no dependence of θ_{3D} on F_{disk} for $F_{disk} > 0.2$. Moreover, theoretically, the alignment between galaxies and their host halos is expected to be influenced by their formation history. Galaxies formed mainly by mergers should have more similar formation history as their host halos. Therefore, we think F_{acc} might be a more fundamental property related to galaxy–halo alignment.

To prove this hypothesis, we investigate whether the dependence of θ_{3D} on the other parameters can be eliminated when controlling F_{acc}. Hence, after dividing the galaxies into 10 equal subsamples according to F_{acc}, we further divide the galaxies into five equal subsamples sorted by M_{vir} in each F_{acc} bins. We show the mean $\cos(\theta_{3D})$ of each M_{vir} subsample in each F_{acc} bin in Figure 8. We find that after binning by F_{acc}, the major and median axes show almost no dependence on M_{vir} for all redshifts. However, for the minor axis, there is still a weak dependence on M_{vir}, but in the opposite direction to the trend shown in Figure 7 where larger M_{vir} galaxies exhibit smaller mean $\cos(\theta_{3D})$. This opposite dependence also appears to be present for the major and median axes, but to a much lesser extent.

The results presented in Figures 7 and 8 suggest that F_{acc} is a crucial parameter for characterizing galaxy–halo alignment. However, additional dependences of the mean $\cos(\theta_{3D})$ on redshift or M_{vir} after controlling for F_{acc} suggests the possibility of a secondary parameter affecting the alignment. Specifically, as demonstrated in Figures 7 and 8, after binned by F_{acc}, the dependence of θ_{3D} on redshift and M_{vir} is nearly negligible for galaxies formed predominantly through mergers ($F_{acc} > 0.5$). In contrast, galaxies formed primarily in situ ($F_{acc} < 0.5$) exhibit a clear dependence on redshift and M_{vir}. This dependence may arise from the differences in the star formation and feedback processes experienced by galaxies at different redshifts and with varying host halo masses, which can potentially impact the galaxy–halo alignment. Additionally, we should exercise caution regarding the definition of F_{acc}, as it may not be equitable across different redshifts and galaxies. This discrepancy can lead to nonuniversal behavior. Further investigation is required to elucidate these effects fully.

4.2. 2D Misalignment Angle

We follow a similar approach as in 3D to study the dependence of 2D misalignment on different galaxy and halo properties. In Figure 9, we show the mean $|\theta_{2D}|$ obtained from the best-fit TSE distributions. We find similar trends as in 3D, where the mean $|\theta_{2D}|$ decreases with F_{acc}, M_{vir}, and M_*, and increases with F_{disk} and redshift. However, we observe that the scatter between different redshifts is much larger compared to that in 3D. Specifically, for F_{acc}, although $|\theta_{2D}|$ also shows weak dependence on redshift at $F_{acc} > 0.5$, the scatter at $F_{acc} < 0.5$ is larger than in 3D.

The larger difference in $|\theta_{2D}|$ between different redshifts can be attributed to the evolution of galaxy and halo shapes. The orientation of the 2D major axis is determined by all three 3D principle axes, and the contribution of each 3D axis depends on

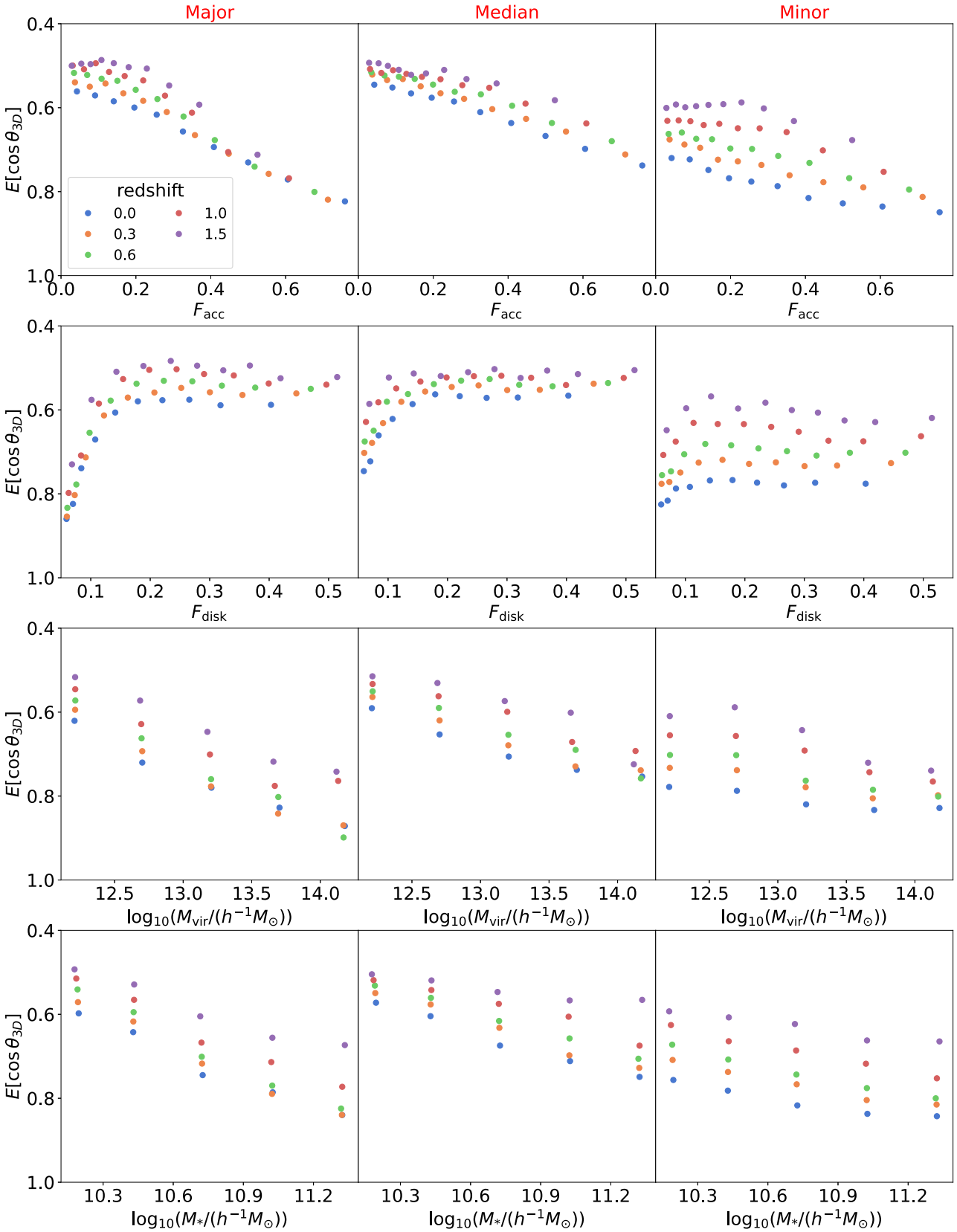

Figure 7. The mean $\cos(\theta_{3D})$ for galaxies binned by different properties and at different redshifts. Each column shows the results for one principle axis and each row shows the results for the same property. Results from different redshifts are displayed by different colors. All the properties are plotted with the mean value in each bin.

the axial ratios c/a and b/a. Therefore, even if θ_{3D} remains constant with redshift, changes in axial ratios with redshift can cause θ_{2D} to show a dependence on redshift, as it contains different contributions from the three principle axes with different θ_{3D}. We verify the above conjecture by recalculating the 2D misalignment angles $|\theta_{2D}^{major}|$, where the 2D major axes of

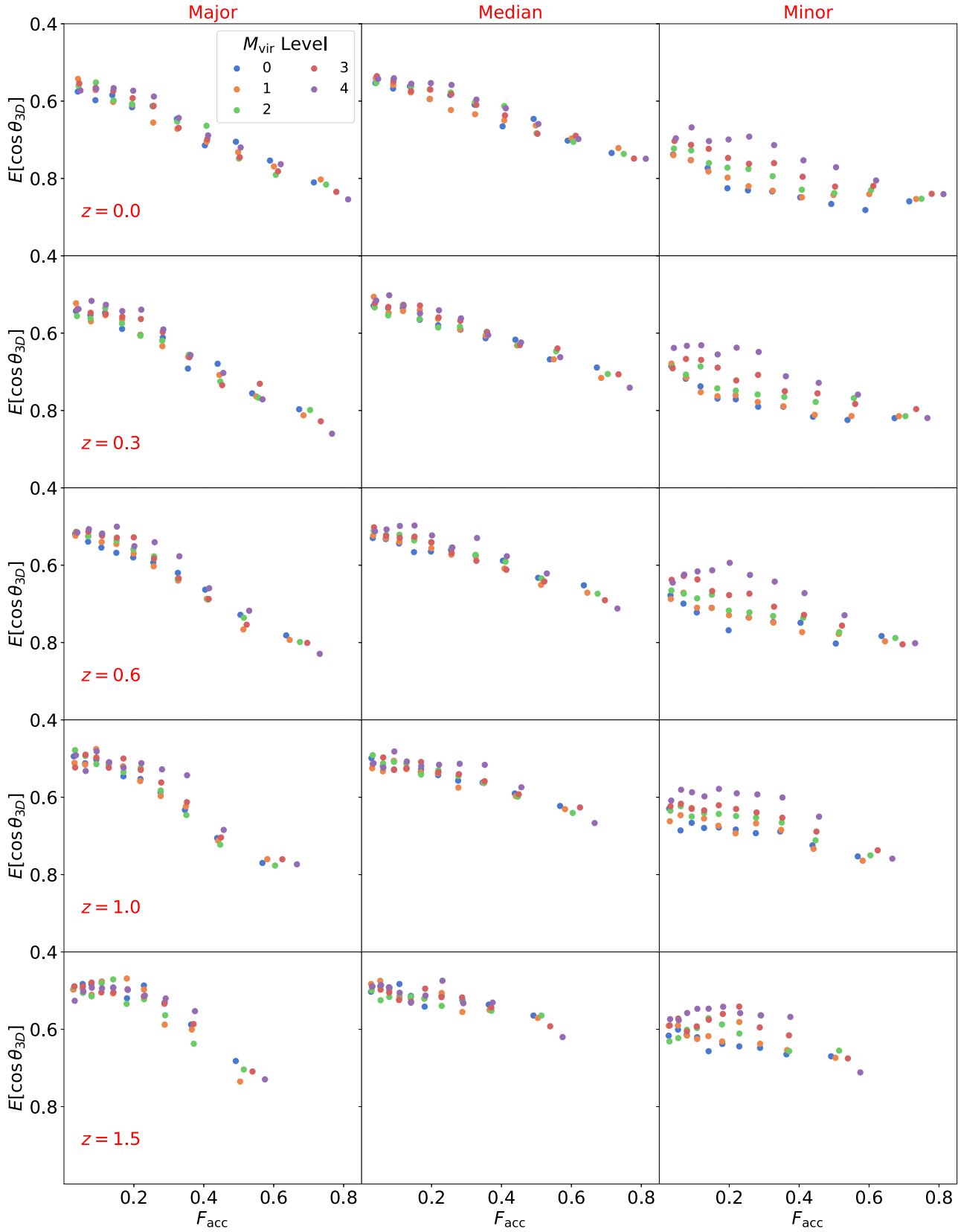

Figure 8. The mean $\cos(\theta_{3D})$ for galaxies binned first by $F_{\rm acc}$ and further by $M_{\rm vir}$. Galaxies at each redshift are first divided into 10 equal subsamples sorted by $F_{\rm acc}$. In each $F_{\rm acc}$ bin, they are further divided into five equal subsamples sorted by $M_{\rm vir}$. Different $M_{\rm vir}$ bins in each $F_{\rm acc}$ bin are plotted with different colors, with 0 indicating the lowest $M_{\rm vir}$ and 4 indicating the highest. Each column shows the results for one principle axis and each row shows the results for the same redshift. All results are plotted with the mean $F_{\rm acc}$ in each bin.

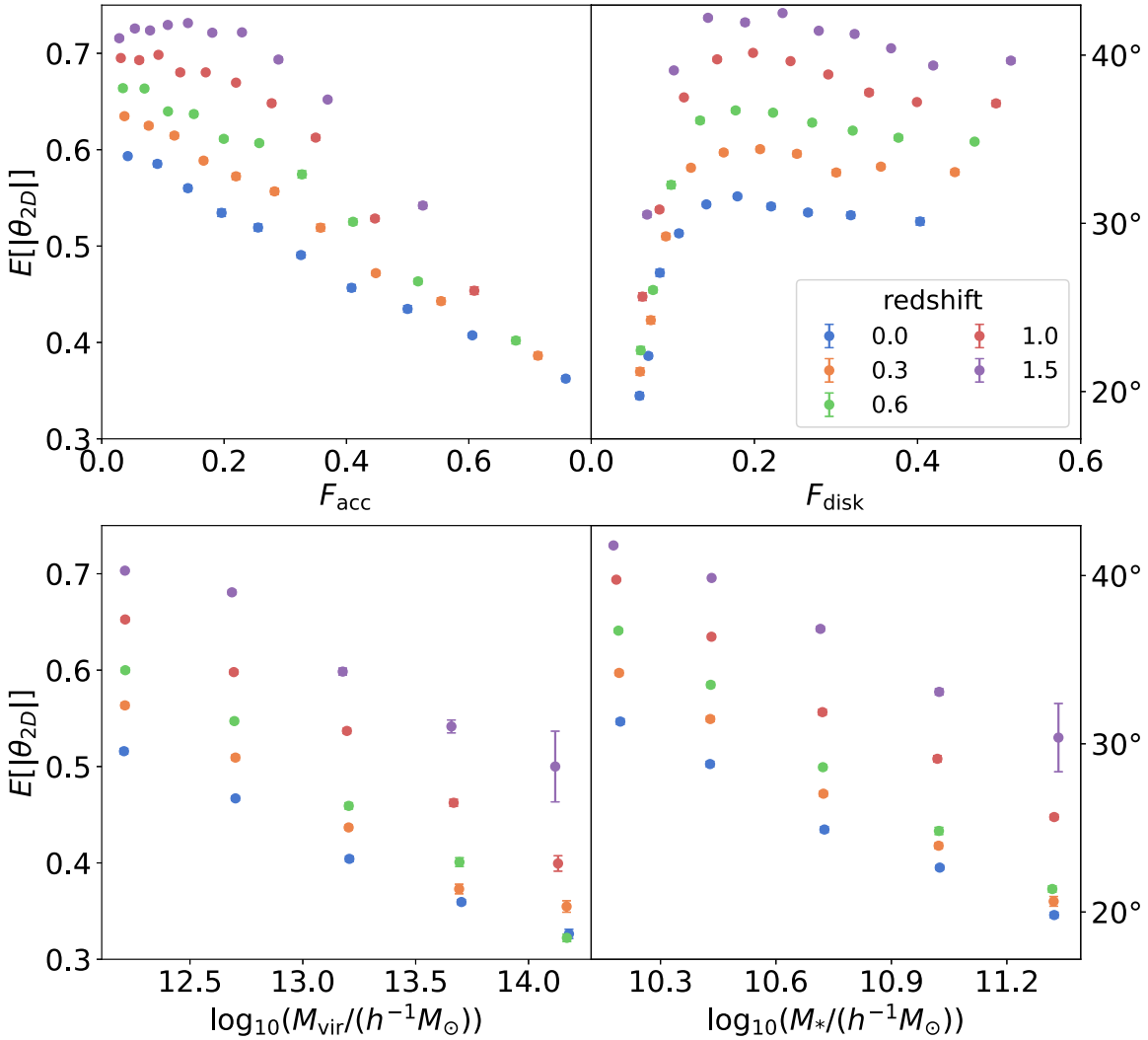

Figure 9. The mean $|\theta_{2D}|$ of galaxies binned by different properties and at different redshifts. Results from different redshifts are displayed by different colors. All the properties are plotted with the mean value in each bin.

the galaxies and halos are obtained from projections of the 3D major axes, which is equivalent to assuming that a galaxy or halo is a line along its major axis with $c/a = 0$ and $b/a = 0$. In this case, the shape evolution is eliminated. The results are shown in Figure 10. Comparing to $|\theta_{2D}|$, we find that the difference in mean $|\theta_{2D}^{\rm major}|$ between different redshifts is reduced, and the results are consistent with those from the mean $\cos(\theta_{3D})$ of the 3D major axis.

We further calculate the difference $|\theta - \theta^{\rm major}|$ between the orientations of the 2D major axes obtained by projecting all particles θ and only the 3D major axes $\theta^{\rm major}$, and analyze their dependence on the axial ratios. We calculate the mean $|\theta - \theta^{\rm major}|$ and axis ratios b/a and c/a for galaxies and halos binned by $F_{\rm acc}$. As shown in Figure 11, $|\theta - \theta^{\rm major}|$ increases monotonously with b/a for both galaxies and halos. However, the slopes are slightly different for galaxies and halos, which may be due to their different distributions of c/b at fixed b/a. We observe a similar relationship between $|\theta - \theta^{\rm major}|$ and c/a for halos, while galaxies exhibit a different dependence. This indicates that there is a strong relationship with b/a and c/a for halos, while galaxies can have a more complex distribution of shapes. The tight relationship between $|\theta - \theta^{\rm major}|$ and b/a suggests that the evolution of b/a is the primary factor driving the larger differences in mean $|\theta_{2D}|$ between different redshifts, with the behavior of c/a acting as a secondary factor.

Therefore, although we observe a similar dependence in 2D, we believe that studying the galaxy–halo alignment in 3D is much more informative.

5. Conclusion and Discussion

In this study, we investigate the alignment between galaxies and their host halos in both 3D and 2D using the TNG300 simulation. Our goal is to propose a model that can be used to constrain the alignment of galaxies and their host halos in observational studies and understand the physical origin of the galaxy–halo alignment. Our main findings are as follows.

1. The distribution of $|\theta_{2D}|$ can be well described by a TSE distribution across different galaxy and halo properties and at different redshifts.
2. With the TSE distribution, we can reproduce the galaxy GI correlation $\tilde{w}_{g+}$ from halos with only a small bias ($<3°$). This bias may come from the unknown coupling between θ_{2D} and other factors such as halo shape.

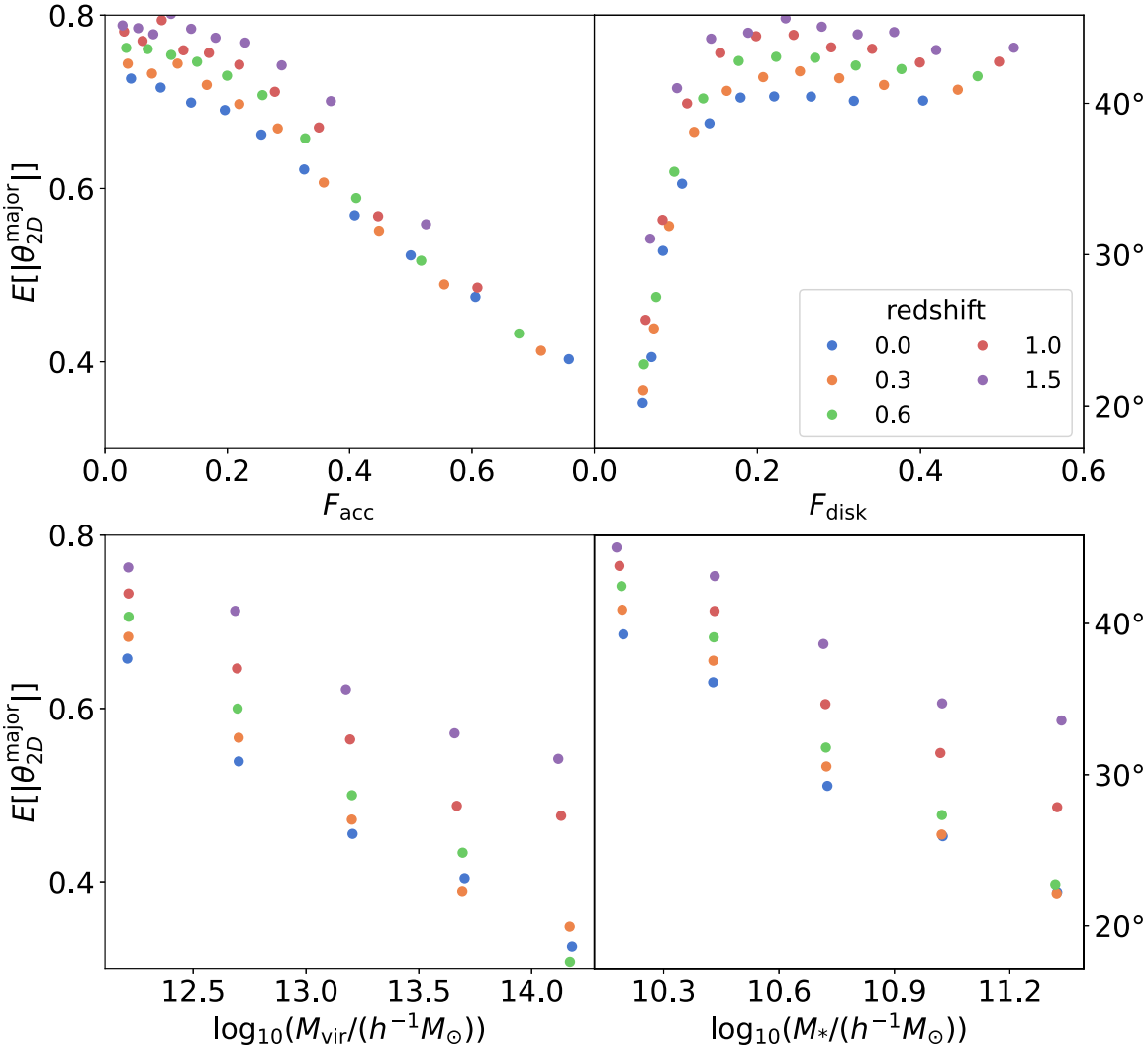

Figure 10. The mean $|\theta_{2D}^{major}|$ from the projection of only 3D major axes rather than all particles. Galaxies are binned by different properties and at different redshifts. Results from different redshifts are displayed by different colors. All the properties are plotted with the mean value in each bin.

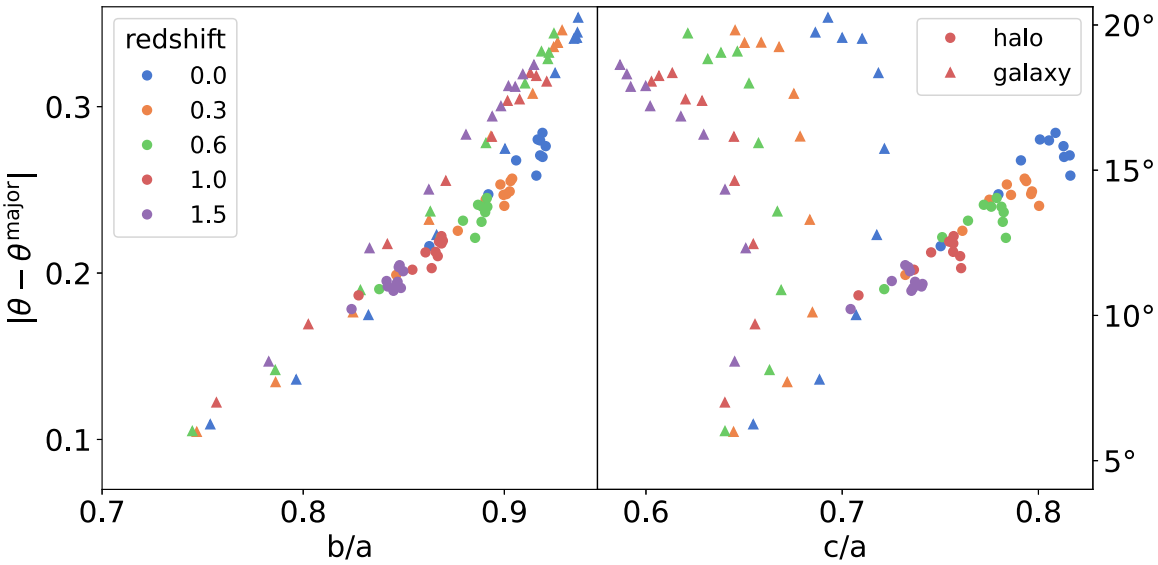

Figure 11. Difference between the position angles of the 2D major axes obtained by projecting all particles θ and only 3D major axes θ^{major} of galaxies and halos, as a function of the mean axis ratios b/a (left) and c/a (right). Galaxies and halos are binned by F_{acc} at each redshift. Results from different redshifts are displayed by different colors, with dots for halos and triangles for galaxies.

3. The 3D misalignment angles θ_{3D} for all three principal axes and the 2D misalignment angles θ_{2D} decrease with F_{acc}, M_{vir}, and M_*, and increase with F_{disk} and redshift, similar to those found by Xu et al. (2023a) from observations.
4. F_{acc} appears to be a more fundamental parameter that determines galaxy–halo alignment than the other parameters we studied. Grouping galaxies by F_{acc}, the M_{vir} dependence of θ_{3D} for all three principle axes is either eliminated or inverted. Moreover, the redshift dependence is also reduced compared to other properties.
5. The redshift dependence of θ_{2D} is much larger than θ_{3D}, which may be due to the evolution of the 3D axis ratios b/a and c/a of both galaxies and halos. In detail, the θ_{3D} of the three principle axes contribute differently to θ_{2D} at different redshift since galaxies and halos have different shape distributions.

Although we have made significant progress in understanding galaxy–halo alignment, there are still some remaining questions that require further investigation. First, it would be interesting to investigate the origin of the remaining dependence on redshift and other properties of θ_{3D} after controlling F_{acc}. Second, it is important to eliminate the small bias in modeling the galaxy GI correlation. Third, our study only considers the orientations of galaxies and halos. Further research is needed to explore the galaxy–halo shape relation and correlations between shapes and orientations to understand the IA fully. Lastly, it is essential to investigate the robustness of our results to the galaxy formation models used in the hydrodynamic simulations, and to test our conclusions with other simulations.

Furthermore, by combining the measurements of GI correlations (Xu et al. 2023a), the galaxy–halo connection (Xu et al. 2023c), the halo IA model (Xia et al. 2017), and the galaxy–halo alignment model developed in this study, it becomes possible to model the IA of central galaxies using a halo model approach.

Our results in this work can enhance the understanding of galaxy–halo alignment and have important implications for IA correction in weak lensing studies, IA cosmology, and the theory of galaxy formation.

Acknowledgments

The work is supported by NSFC (12133006, 11890691, and 11621303), grant No. CMS-CSST-2021-A03, and 111 project No. B20019. We gratefully acknowledge the support of the Key Laboratory for Particle Physics, Astrophysics and Cosmology, Ministry of Education. This work made use of the Gravity Supercomputer at the Department of Astronomy, Shanghai Jiao Tong University.

Appendix A
Generating Random Numbers for the TSE Distribution

To generate random numbers for the TSE distribution from a uniform distribution $U(0, 1)$, we can use the following method. Let X be a random variable following $U(0, 1)$, and we want to find a function y such that $Y = y(X)$ follows a TSE distribution. The cumulative distribution functions of X and Y have the relation $F_X(x) = F_Y(y)$, which leads to the following equation

$$\begin{aligned} x &= \int_0^y (Ae^{-y'/\tau} + B)dy' \\ &= \tau A(1 - e^{-y/\tau}) + By. \end{aligned} \tag{A1}$$

Then, we can solve for $y(x)$ by inverting the above equation as follows

$$z = \frac{A}{B}\exp\left(\frac{A\tau - x}{B\tau}\right), \tag{A2}$$

$$y = \tau W_0(z) - \frac{A\tau - x}{B}. \tag{A3}$$

Finally, we can generate random numbers following the TSE distribution by computing $y(X)$.

Appendix B
The Sum of Exponential Functions

We test the self-consistency of our TSE model by demonstrating that the sum of exponential functions with close exponents τ can also be well fitted by an exponential function. Figure B1 shows the cases where two or three exponential functions with different exponents τ are summed up, and we find that the sum can also be well fitted by an exponential function.

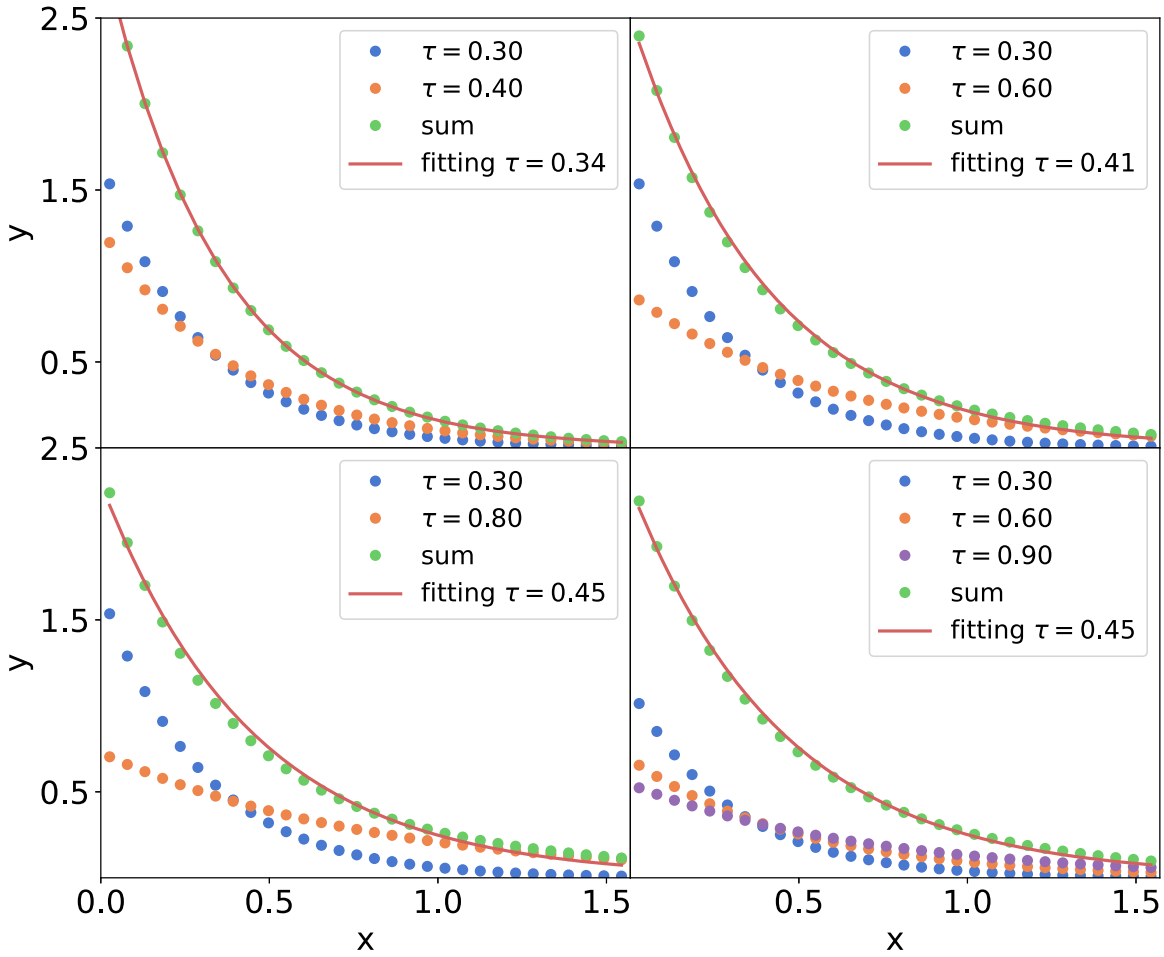

Figure B1. We demonstrate that the sum of exponential functions with similar exponents τ can also be effectively approximated by a single exponential function. All exponential functions are normalized within the interval $[0, \pi/2]$. In cases where n exponential functions are summed up, all the exponential functions being summed are divided by n.

ORCID iDs

Kun Xu https://orcid.org/0000-0002-7697-3306
Y. P. Jing https://orcid.org/0000-0002-4534-3125

References

Alam, S., Albareti, F. D., Allende Prieto, C., et al. 2015, ApJS, 219, 12
Bailin, J., & Steinmetz, M. 2005, ApJ, 627, 647
Bernstein, G. M., & Jarvis, M. 2002, AJ, 123, 583
Bhowmick, A. K., Chen, Y., Tenneti, A., Di Matteo, T., & Mandelbaum, R. 2020, MNRAS, 491, 4116
Blazek, J., McQuinn, M., & Seljak, U. 2011, JCAP, 2011, 010
Blazek, J. A., MacCrann, N., Troxel, M. A., & Fang, X. 2019, PhRvD, 100, 103506
Brown, M. L., Taylor, A. N., Hambly, N. C., & Dye, S. 2002, MNRAS, 333, 501
Bryan, G. L., & Norman, M. L. 1998, ApJ, 495, 80
Catelan, P., Kamionkowski, M., & Blandford, R. D. 2001, MNRAS, 320, L7
Chisari, N., Laigle, C., Codis, S., et al. 2016a, MNRAS, 461, 2702
Chisari, N. E., & Dvorkin, C. 2013, JCAP, 2013, 029
Chisari, N. E., Dvorkin, C., Schmidt, F., & Spergel, D. N. 2016b, PhRvD, 94, 123507
Chisari, N. E., Koukoufilippas, N., Jindal, A., et al. 2017, MNRAS, 472, 1163
Corless, R. M., Gonnet, G. H., Hare, D. E., Jeffrey, D. J., & Knuth, D. E. 1996, AdCoM, 5, 329
Croft, R. A. C., & Metzler, C. A. 2000, ApJ, 545, 561
Davis, M., Efstathiou, G., Frenk, C. S., & White, S. D. M. 1985, ApJ, 292, 371
Dey, A., Schlegel, D. J., Lang, D., et al. 2019, AJ, 157, 168
Dubois, Y., Peirani, S., Pichon, C., et al. 2016, MNRAS, 463, 3948
Faltenbacher, A., Li, C., White, S. D. M., et al. 2009, RAA, 9, 41
Genel, S., Fall, S. M., Hernquist, L., et al. 2015, ApJL, 804, L40
Heavens, A., Refregier, A., & Heymans, C. 2000, MNRAS, 319, 649
Hirata, C. M., Mandelbaum, R., Ishak, M., et al. 2007, MNRAS, 381, 1197
Hirata, C. M., Mandelbaum, R., Seljak, U., et al. 2004, MNRAS, 353, 529
Hirata, C. M., & Seljak, U. 2004, PhRvD, 70, 063526
Hoffmann, K., Secco, L. F., Blazek, J., et al. 2022, PhRvD, 106, 123510
Jagvaral, Y., Singh, S., & Mandelbaum, R. 2022, MNRAS, 514, 1021
Jing, Y. P. 2002, MNRAS, 335, L89
Jing, Y. P., Mo, H. J., Borner, G., & Fang, L. Z. 1995, MNRAS, 276, 417
Jing, Y. P., & Suto, Y. 2002, ApJ, 574, 538
Katz, N. 1991, ApJ, 368, 325
Khandai, N., Di Matteo, T., Croft, R., et al. 2015, MNRAS, 450, 1349
Kirk, D., Brown, M. L., Hoekstra, H., et al. 2015, SSRv, 193, 139
Kirk, D., Rassat, A., Host, O., & Bridle, S. 2012, MNRAS, 424, 1647
Kogai, K., Matsubara, T., Nishizawa, A. J., & Urakawa, Y. 2018, JCAP, 2018, 014
Krause, E., Eifler, T., & Blazek, J. 2016, MNRAS, 456, 207
Kurita, T., & Takada, M. 2023, arXiv:2302.02925
Landy, S. D., & Szalay, A. S. 1993, ApJ, 412, 64
Li, C., Jing, Y. P., Faltenbacher, A., & Wang, J. 2013, ApJL, 770, L12
Mandelbaum, R., Hirata, C. M., Ishak, M., Seljak, U., & Brinkmann, J. 2006, MNRAS, 367, 611
Marinacci, F., Vogelsberger, M., Pakmor, R., et al. 2018, MNRAS, 480, 5113
Naiman, J. P., Pillepich, A., Springel, V., et al. 2018, MNRAS, 477, 1206
Nelson, D., Pillepich, A., Springel, V., et al. 2018, MNRAS, 475, 624
Nelson, D., Springel, V., Pillepich, A., et al. 2019, ComAC, 6, 2
Okumura, T., & Jing, Y. P. 2009, ApJL, 694, L83
Okumura, T., Jing, Y. P., & Li, C. 2009, ApJ, 694, 214
Okumura, T., & Taruya, A. 2020, MNRAS, 493, L124
Okumura, T., & Taruya, A. 2022, PhRvD, 106, 043523

Okumura, T., & Taruya, A. 2023, ApJL, 945, L30
Okumura, T., Taruya, A., & Nishimichi, T. 2020, MNRAS, 494, 694
Pen, U.-L., Lee, J., & Seljak, U. 2000, ApJL, 543, L107
Pillepich, A., Nelson, D., Hernquist, L., et al. 2018a, MNRAS, 475, 648
Pillepich, A., Springel, V., Nelson, D., et al. 2018b, MNRAS, 473, 4077
Planck Collaboration, Ade, P. A. R., Aghanim, N., et al. 2016, A&A, 594, A13
Reid, B., Ho, S., Padmanabhan, N., et al. 2016, MNRAS, 455, 1553
Rodriguez, F., Merchán, M., & Artale, M. C. 2022, MNRAS, 514, 1077
Rodriguez-Gomez, V., Genel, S., Vogelsberger, M., et al. 2015, MNRAS, 449, 49
Rodriguez-Gomez, V., Pillepich, A., Sales, L. V., et al. 2016, MNRAS, 458, 2371
Samuroff, S., Mandelbaum, R., Blazek, J., et al. 2022, MNRAS, 524, 2195
Schaye, J., Crain, R. A., Bower, R. G., et al. 2015, MNRAS, 446, 521
Schaye, J., Dalla Vecchia, C., Booth, C. M., et al. 2010, MNRAS, 402, 1536
Schmidt, F., Chisari, N. E., & Dvorkin, C. 2015, JCAP, 2015, 032
Schneider, M. D., & Bridle, S. 2010, MNRAS, 402, 2127
Sheng, M.-J., Yu, H.-R., Li, S., et al. 2023, ApJ, 943, 128
Singh, S., Mandelbaum, R., & More, S. 2015, MNRAS, 450, 2195
Springel, V. 2010, MNRAS, 401, 791
Springel, V., Pakmor, R., Pillepich, A., et al. 2018, MNRAS, 475, 676
Springel, V., White, S. D. M., Tormen, G., & Kauffmann, G. 2001, MNRAS, 328, 726
Tenneti, A., Mandelbaum, R., & Di Matteo, T. 2016, MNRAS, 462, 2668
Tenneti, A., Mandelbaum, R., Di Matteo, T., Feng, Y., & Khandai, N. 2014, MNRAS, 441, 470
The Dark Energy Survey Collaboration 2005, arXiv:astro-ph/0510346
Velliscig, M., Cacciato, M., Schaye, J., et al. 2015, MNRAS, 453, 721
Weinberger, R., Springel, V., Hernquist, L., et al. 2017, MNRAS, 465, 3291
Xia, Q., Kang, X., Wang, P., et al. 2017, ApJ, 848, 22
Xu, K., Jing, Y. P., & Gao, H. 2023a, ApJ, 954, 2
Xu, K., Jing, Y. P., Zhao, G.-B., & Cuesta, A. J. 2023b, arXiv:2306.09407
Xu, K., Jing, Y. P., Zheng, Y., & Gao, H. 2023c, ApJ, 944, 200
Yang, X., van den Bosch, F. C., Mo, H. J., et al. 2006, MNRAS, 369, 1293
Yao, J., Shan, H., Zhang, P., Kneib, J.-P., & Jullo, E. 2020, ApJ, 904, 135
York, D. G., Adelman, J., & Anderson, J. E., Jr. 2000, AJ, 120, 1579